

Axion Topology in Photonic Crystal Domain Walls

Chiara Devescovi^{*,1,*}, Antonio Morales-Pérez^{*,1}, Yoonseok Hwang,² Mikel García-Díez,^{1,3} Iñigo Robredo,^{4,1} Juan Luis Mañes,³ Barry Bradlyn,² Aitzol García-Etxarri,^{1,5,†} and Maia G. Vergniory^{4,1,‡}

¹*Donostia International Physics Center, Paseo Manuel de Lardizabal 4, 20018 Donostia-San Sebastian, Spain.*

²*Department of Physics, University of Illinois at Urbana-Champaign, Urbana, IL, USA*

³*Physics Department, University of the Basque Country (UPV/EHU), Bilbao, Spain*

⁴*Max Planck Institute for Chemical Physics of Solids, Dresden D-01187, Germany*

⁵*IKERBASQUE, Basque Foundation for Science, María Díaz de Haro 3, 48013 Bilbao, Spain.*

(Dated: June 1, 2023)

Axion insulators are 3D magnetic higher-order topological insulators protected by inversion-symmetry that exhibit hinge-localized chiral channels and induce quantized topological magnetoelectric effects. Recent research has suggested that axion insulators may be capable of detecting dark-matter axion-like particles by coupling to their axionic excitations. Beyond its fundamental theoretical interest, designing a photonic AXI offers the potential to enable the development of magnetically-tunable photonic switch devices through the manipulation of the axionic modes and their chiral propagation using external magnetic fields. Motivated by these facts, in this work, we propose a novel approach to induce axionic band topology in gyrotropic 3D Weyl photonic crystals gapped by supercell modulation. To quantize an axionic angle, we create domain-walls across inversion-symmetric photonic crystals, incorporating a phase-obstruction in the supercell modulation of their dielectric elements. This allows us to bind chiral channels on inversion-related hinges, ultimately leading to the realization of an axionic chiral channel of light. Moreover, by controlling the material gyrotropic response, we demonstrate a physically accessible way of manipulating the axionic modes through a small external magnetic bias, which provides an effective topological switch between different 1D chiral photonic fiber configurations. Remarkably, the unidirectional axionic hinge states supported by the photonic axion insulator are buried in a fully connected 3D dielectric structure, thereby being protected from radiation through the electromagnetic continuum. As a result, they are highly suitable for applications in guided-light communication, where the preservation and non-reciprocal propagation of photonic signals are of paramount importance.

INTRODUCTION

Axion insulators (AXIs) [1–19] are 3D inversion (\mathcal{I})-symmetric magnetic higher-order topological insulators (HOTIs) [20, 21] which induce various topological magnetoelectric effects, such as the quantized magneto-optical Faraday and Kerr rotation, the image magnetic monopole effect, and half-quantized surface Hall conductance [7–10]. The topological properties of AXIs arise from the quantization of their electromagnetic coupling term, the so-called topological θ -angle [1–3], which is pinned to π in presence of \mathcal{I} -symmetry (or other θ -odd operations such as roto-inversions and time-reversed rotations). [22].

AXIs are of significant interest because, acting as HOTI, they are able to support hinge-localized chiral modes, which propagate in the form of unidirectional axionic channels [23–25]. These hinge-states are expected to emerge at the 1D facets of an AXI crystal-lite or in the presence of 1D dislocations in the AXI lattice, where gradients of the θ angle arise, inducing the formation of axionic strings [10, 24, 26]. Recent studies [10, 16] have shown that the chiral propagation of the AXI hinge-localized modes is highly-tunable. Especially in the presence of a ferromagnetic order, it is possible to switch between different hinge-modes configurations via external magnetic control, allowing magnetic re-routing of conducting channels from one input into

one or more outputs. In the context of Photonic Crystals (PhCs), this remarkable property of AXIs could allow for devices that manipulate, direct and deviate the 1D non-reciprocal flow of light, with relevant applications for optical communication technologies and for the development of magnetically-tunable photonic switch devices. Until now, no proposals have been presented for axion-based PhCs or axion-protected light propagation. Furthermore, recent studies have suggested the use of AXI materials for detecting axion-like particles, that constitute dark-matter candidates [27–29]. This is due to the fact that emergent axionic excitations in AXI couple with electromagnetism, $\mathcal{L} \propto \theta \mathbf{E} \cdot \mathbf{B}$, similar to the axion-photon coupling observed in high-energy physics for light dark-matter, which follows $\mathcal{L} \propto a \mathbf{E} \cdot \mathbf{B}$. In PhCs, photons can interact with external magnetic fields via gyrotropy, they display a non-zero effective mass, and they are wavelength-tunable via lattice size-scaling, all of which are essential ingredients for the realization of an axion haloscope [27, 30–32]. The demonstration of an AXI in a PhC could represent an opportunity to bridge these two different approaches in the study of axion-photon coupling.

Despite the theoretical significance and potential applications of AXIs, no proposals have yet been put forward for their implementation in PhCs: our work aims to propose and demonstrate the first theoretical model and

general design strategy for photonic AXIs in 3D PhCs. To induce a photonic axionic band topology, we incorporate a phase-obstruction in the Supercell Modulation (SM) of the dielectric elements within gyrotropic Weyl PhCs [33, 34]. The SM is designed as an \mathcal{I} -symmetric, static, geometric deformation of the PhC lattice, enabling an experimental implementation of the PhC without necessitating any dynamic driving. Serving as a photonic analog of a charge-density-wave (CDW) [25, 35–37], the SM couples Weyl points with opposite topological charges while maintaining the \mathcal{I} -symmetry of the model.

The resulting AXI is dubbed *relative*, because it is only exhibited at the interface of two PhCs with a quantized *relative* axionic angle $\delta\theta$ and vanishing *relative* Chern numbers. This approach is grounded in the concept that a dislocation of the CDW phase in a specific class of \mathcal{I} -symmetric Weyl semimetals (WS) acts as a dynamic axion field [25, 26, 35]. Consequently, the domain-wall separating the phase-obstructed CDW-WS can be interpreted as the critical point between a trivial insulator and an AXI. By employing this strategy, we successfully realize a photonic *relative* axion insulator (*r*AXI) in a realistic gyrotropic setup.

By inserting planar dislocations in the dielectric modulation phase, we bind 1D chiral channels on \mathcal{I} -related hinges, that provide a PhC realization of an axion domain wall protected by \mathcal{I} -symmetry.

Remarkably, the 1D channels supported by the PhC are buried in a fully connected 3D dielectric structure, thus protected from radiation through the electromagnetic continuum [38]. This design not only represents the first instance of a tunable HOTI with chiral hinge states in 3D PhCs [39], but the observed 1D-modes are also consistent with a single, unidirectional axionic channel that wraps around the central phase-obstructed core, endowing the photonic hinge-channels with non-reciprocal propagation properties.

Lastly, we propose a physically viable method for manipulating these axionic hinge modes by controlling the PhC gyrotropic response using a small external magnetic bias. Specifically, we induce gyrotropy-induced transitions in the photonic AXI, which function as an efficient topological switch between various 1D photonic fiber configurations. Interestingly, recent experimental advancements in 3D gyrotropic crystals have demonstrated that imparting a magnetic response to 3D photons is possible, with a high degree of control and intensity [40, 41]. These findings suggest that it may be possible to manipulate, direct, and deviate the 1D non-reciprocal flow of light in a photonic AXI using state-of-the-art experimental setups. The capability of manipulating the HOTI hinge states in the photonic AXI via gyrotropy underscores the potential of the proposed design for creating magnetically-tunable photonic switch devices, thereby paving the way for advancements in axion-based photonics.

The main body of the manuscript is divided into three

sections: In Section 1, we provide the bulk design and topological characterization of the photonic *relative* axion insulator (*r*AXI); In Section 2, we show how to make *r*AXI topology manifest by creating a domain-wall between phase-obstructed \mathcal{I} -symmetric *r*AXIs; In Section 3, we demonstrate how to generate and manipulate the higher order topology of the PhC, by controlling the chiral propagation of the axionic channels of light. Finally, in the Methods Section, we show how to efficiently simulate the electromagnetic response of the *r*AXI, via a transversality-enforced tight-binding model (TETB) [42]. This model is capable of capturing and regularizing the Γ -point electromagnetic obstruction that arises in 3D PhCs, due to the transversality constraint of the Maxwell equations [42, 43].

RESULTS

1. Relative axion topology

Our starting setup for inducing photonic AXI band topology consists of an \mathcal{I} -symmetric gyrotropic PhC [34, 42, 44] under an external magnetic field $\mathbf{H} = (0, 0, H_z)$, as shown in Fig. 1(a).

In the presence of a gyroelectric medium the external magnetic field induces an off-diagonal imaginary component in the permittivity tensor [45, 46], as expressed by the following equation:

$$\varepsilon_{\eta_z} = \begin{pmatrix} \varepsilon_{\perp} & i\eta_z & 0 \\ -i\eta_z & \varepsilon_{\perp} & 0 \\ 0 & 0 & \varepsilon \end{pmatrix}, \quad (1)$$

where $\eta_z = \eta_z(H_z)$ is the bias-dependent gyroelectric parameter with $\varepsilon_{\perp} = \sqrt{\varepsilon^2 + \eta_z^2}$ and ε the dielectric constant (here $\varepsilon = 16$). As a consequence of time-reversal symmetry (TRS) breaking due to gyrotropy, a photonic Weyl dipole is generated in the Brillouin zone, along the direction of the H_z magnetic field, as shown in Fig. 1(a). In the case of this dielectric lattice realization, the Weyl dipole separation increases proportionally to the external H_z and can be magnetically tuned.

In order to emulate the effect of a CDW in condensed-matter systems [23, 25, 36] to open a topological gap, we introduce a z -directed SM of lattice period $N \in \mathbb{N}$ and $N \geq 2$, commensurate with the Weyl dipole separation $\mathbf{Q} = \mathbf{q}_+ - \mathbf{q}_-$, where \mathbf{q}_{\pm} are the locations of Weyl points with chirality ± 1 in Brillouin zone. Accordingly, we fix the Weyl points of opposite topological charge at approximately $\mathbf{q}_{\pm} = (\pi, \pi, \pi \pm \pi/N)$. This results in a folding of the BZ, as shown in Fig. 1(b), and couples the Weyl points to open a non-trivial gap, as shown in Fig. 1(c).

The SM is introduced as a local deformation δr of the radius r of the dielectric rods, according to the relation:

$$\delta r = r_m \cos(2\pi z/N|a| + \phi),$$

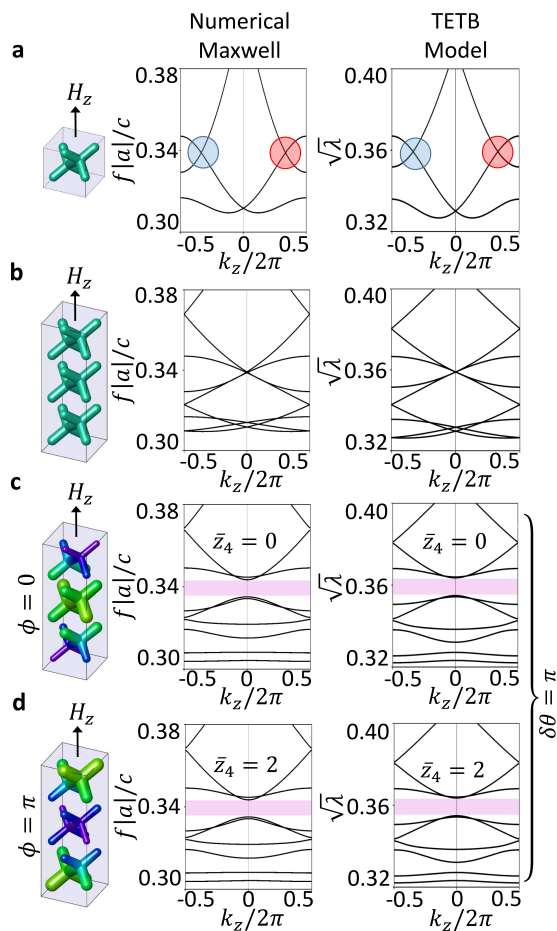


FIG. 1. Effect of a supercell modulation on the photonic Weyl bands. Left panels show the PhC geometry and the reduced frequencies $f|a|/c$, where c is the speed of light and $|a|$ the scale invariant lattice parameter, obtained by solving numerically the Maxwell equations. Right panels show the square-root of the transversality-enforced tight-binding model (TETB) eigenvalues $\sqrt{\lambda}$, consistent with the mapping between the Schrödinger and electromagnetic wave equations, that relates energies and frequencies quadratically ($\lambda \sim \omega^2$, see [42]). In these plots we show the k_z line, for fixed $k_x = \pi$ and $k_y = \pi$. Weyl points which are separated by a $|\mathbf{Q}| = 2\pi/N$ distance in momentum space as in panel (a), are superimposed on an artificial supercell in panel (b), and then coupled by a commensurate SM of period $N = 2\pi/|\mathbf{Q}|$ as in panels (c-d). The supercell amplitude is $r_m/r_0 = 1/20$ for the PhC and $V_{4c} = -V_{4b} = 1/150$ for the TETB. Panel (c) and (d) differ solely for the angular phase of the supercell modulation ϕ , with $\phi = 0$ in panel (c), and $\phi = \pi$ in panel (d).

where $|a|$ is the lattice parameter of the starting photonic crystal, while r_m and ϕ control, respectively, the amplitude and the phase of the dielectric modulation. Note that this represents a static geometric deformation of the PhC structure which can be stably implemented during the fabrication process and does not require any dynamical driving. The ϕ phase of the SM is the fun-

damental design parameter which we will set in order to induce axionic band topology.

For the purpose of preserving the \mathcal{I} -symmetry of the unperturbed PhC of Fig. 1(a), which is crucial for axion behaviour, we pin the modulation at the \mathcal{I} -center and target only two specific values of the SM phase: $\phi = 0$ and $\phi = \pi$. The corresponding modulated dielectric structures are shown in Fig. 1(c-d) in a 3D rendering, and in Fig. 2 in a side view, for a $N = 3$ modulation period. We see that both $\phi = 0$ and $\phi = \pi$ phases display the same insulating spectrum. However, we will now demonstrate that their 3D photonic bulk gaps exhibit a different topological obstruction in the \mathcal{I} -symmetry-indicators associated to the quantization of their *relative* axion angle $\delta\theta$.

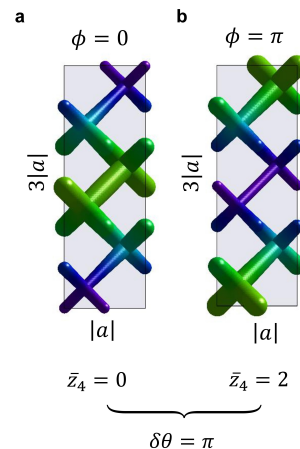


FIG. 2. 3D photonic *r*AXI resulting from a $N = 3$ periodic SM imposed on a gyrotropic Weyl photonic semimetal (side view). The SM acts as a local deformation of the diameter of the dielectric rods. The z -directed modulation is along the magnetization axis. The SM is centered at the inversion center of the unperturbed lattice; panels (a) and (b) correspond to an angular phase ϕ of the SM of 0 and π , respectively.

To efficiently model the electromagnetic response of the PhC, we develop an analytical model of the 3D photonic bulk bands via the transversality-enforced tight-binding model method (TETB) introduced by Ref. [42]. The TETB model is constructed via the introduction of \mathbf{v}^L auxiliary longitudinal modes, able to regularize the Γ -point obstruction arising from the transversality constraint of the Maxwell equations, as proposed in Ref. [43]. The positive-energy solutions of the TETB are mapped to frequency dispersion of the \mathbf{v}^T transverse electromagnetic modes, obtained by numerically solving the Maxwell equation via the MIT Photonic Bands package (MPB) [47]. The SM is introduced in the TETB via a simple onsite supercell-modulated potential, that mimics the local electromagnetic energy redistribution in the modulated dielectric rods (see Methods section):

$$H_{\Delta}(\mathbf{r}, \mathbf{H}) = H(\mathbf{r}, \mathbf{H}) + \sum_i V_i \cos\left(\frac{2\pi z_i}{N|a|} + \phi\right) c_i^{\dagger}(\mathbf{r})c_i(\mathbf{r}), \quad (2)$$

where $H(\mathbf{r}, \mathbf{H})$ is the real-space TETB Hamiltonian for the magnetic system before modulation, $|a|$ is the lattice parameter of the crystal before modulation, and V_i and ϕ parameterize the amplitude and the phase of the modulation, respectively. Note that the sum in Eq. (2) runs over all the basis pseudo-orbitals used in the TETB model. As shown in the Methods section, the TETB reproduces all the bulk properties of the supercell-modulated PhC; a comparison of the respective bands and topology is displayed in Fig. 1.

In order to understand the role of \mathcal{I} -symmetry in protecting the r AXI topology, we compute the magnetic symmetry-indicators (SI) $\nu_{\phi}^T = \{\bar{z}_{2,x}, \bar{z}_{2,y}, \bar{z}_{2,z} | \bar{z}_4\}$ [18, 48–52] for the transverse-electromagnetic modes of the PhC (the $\bar{}$ overbar stands for magnetic and the $()^T$ superscript indicates transverse bands). In particular, we focus our interest on the \bar{z}_4 strong index, which is associated to axion topology [17, 35, 52].

As shown in the Methods section, we obtain, correspondingly for the two structures at $\phi = 0$ and $\phi = \pi$:

$$\nu_{\phi=0}^T = \{0, 0, 1|0\} \quad (3)$$

and

$$\nu_{\phi=\pi}^T = \{0, 0, 1|2\} \quad (4)$$

where the $\delta\bar{z}_4 = 2$ discontinuity of the *even* \bar{z}_4 index stands to indicate a *relative* axionic obstruction. On the other hand, the invariance of the $\bar{z}_{2,z}$ term is related to an odd C_z Chern invariant, which, as confirmed via photonic Wilson loop [33, 53, 54] calculations, is $C_z = 1$ identically for both structures. Note that although we have computed $\nu_{\phi=0}^T$ and $\nu_{\phi=\pi}^T$ using the TETB model, the difference

$$\nu_{\phi=\pi}^T - \nu_{\phi=0}^T = \{0, 0, 0|2\} \quad (5)$$

depends only on the sign of the modulation-induced band gap. We thus find that Eq. (5) holds for the PhC.

To verify the quantization of the *relative* axion angle between $\phi = 0, \pi$, we compute the layer Chern number G_z of a z -slab with its normal along the magnetization axis. As demonstrated in [10, 22], a non-zero quantized axionic phase θ will manifests as an offset in G_z , according to the relation:

$$G_z = C_z n_z + \theta/\pi \quad (6)$$

where n_z counts the layers of the slab. Via this equation, we are able to extract the θ axion angle, from the C_z Chern number of a single layer.

The slab Wilson loops, shown in Fig. 3, wind n_z and $n_z + 1$ times, respectively for $\phi = 0$ and $\phi = \pi$, confirming a $\delta\theta = \pi$ discontinuity in the axion θ angle. Therefore the $\phi = 0, \pi$ supercell-modulated PhC represent r AXI.

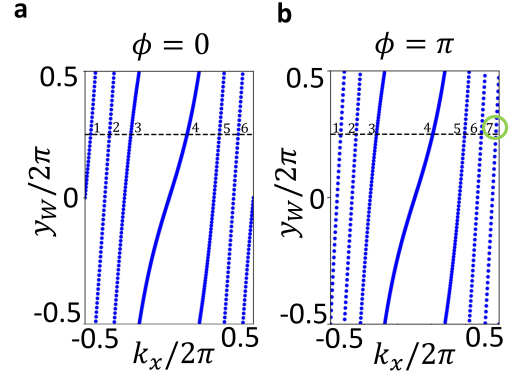


FIG. 3. Layer Wilson loop for a z -slab at $\phi = 0$ (panel a) and $\phi = \pi$ (panel b) with $n_z = 6$ layers. The y Wannier energy centers wind respectively n_z and $n_z + 1$ times along k_x , with the $+1$ discontinuity shown in the green circle. This confirms a $\delta\theta = \delta\phi = \pi$ difference in the *relative* axion angle.

2. Phase-obstructed domain walls

In this section, our goal is to manifest the *relative* axion topology. To accomplish this, we create a domain-wall in x between the photonic 3D insulator with $\phi = 0$ and its obstructed counterpart with $\phi = \pi$, i.e. imposing a *relative* axion phase difference of $\delta\theta \equiv \delta\phi = \pi$, as shown in Fig. 4(a).

We expect this domain-wall configuration to be formally equivalent to the critical point between an AXI with $\theta = \pi$ and a trivial insulator [25, 26, 35, 55] and therefore gapped. To ensure a surface gap, we apply a small tilt to the z -directed magnetic field, with

$$\mathbf{H} = (|h|\cos(\sigma), |h|\sin(\sigma), H_z)$$

and $|h| \ll |H_z|$. As shown in the Supplementary Notes, the component of the magnetic perturbation normal to the interface plane ensures the existence of a surface gap, which is essential for the observation of the higher-order topology of the r AXI. The tilted external field couples to the PhC, inducing an in-plane gyrotropic perturbation $\eta_{x,y} = \eta_{x,y}(h_{x,y})$ in the permittivity tensor. As result, as shown in Fig. 4(b), the PhC domain-wall bands are gapped.

The size of the surface gap can be controlled via the $h_{x,y}$ bias, by gradually deviating from the gapless condition which results from the boundary condition choice, as demonstrated in the Supplementary Notes. In what follows we choose a boundary condition where the size of the surface gap vanishes in absence of any magnetization orthogonal to the interface plane: this boundary configuration is reached by maintaining the rod geometry continuously connected across interface for the PhC. In the TETB, this correspond to a surface potential that

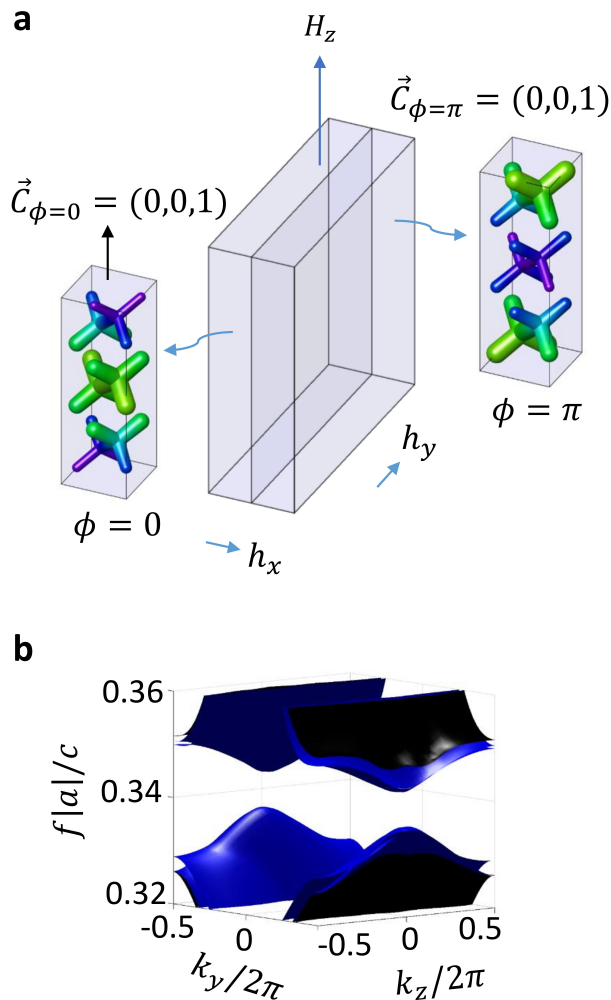


FIG. 4. Axionic surface gap for an \mathcal{I} -symmetric domain-wall with $\delta\theta \equiv \delta\phi = \pi$. In panel (a), PhC geometry of the phase-obstructed domain-wall configuration. In panel (b), domain-wall band structure on the $x = 0$ plane, with projected bulk bands in black, and surface-localized states in blue.

linearly interpolates between the two modulations.

Importantly, the $\phi = 0$ and $\phi = \pi$ structures differ only in their \bar{z}_4 index but have an identical Chern vector. It is critical to maintain the condition of equal Chern vectors across the interface in order to prevent anomalous Hall surface states to populate the surface gap, consistently with vectorial bulk-boundary correspondence [34].

3. Gyrotropy-induced switching of HOTI states

Next, to generate and manipulate a chiral hinge channel of light, we will be investigating the higher-order topology of the PhC. For this purpose, we construct an \mathcal{I} -symmetric z -wire configuration, embedding a $N_x \times N_y$ core of $\phi = 0$ PhC, inside a $2N_x \times 2N_y$ region of PhC of the same material with $\phi = \pi$. The corresponding di-

electric structure, which is fully connected, is shown in Fig. 6(a), with the central rod extruded upwards, for better visualization. To keep the simulations affordable, we compute the boundary modes for this rod-geometry via the use of the TETB model.

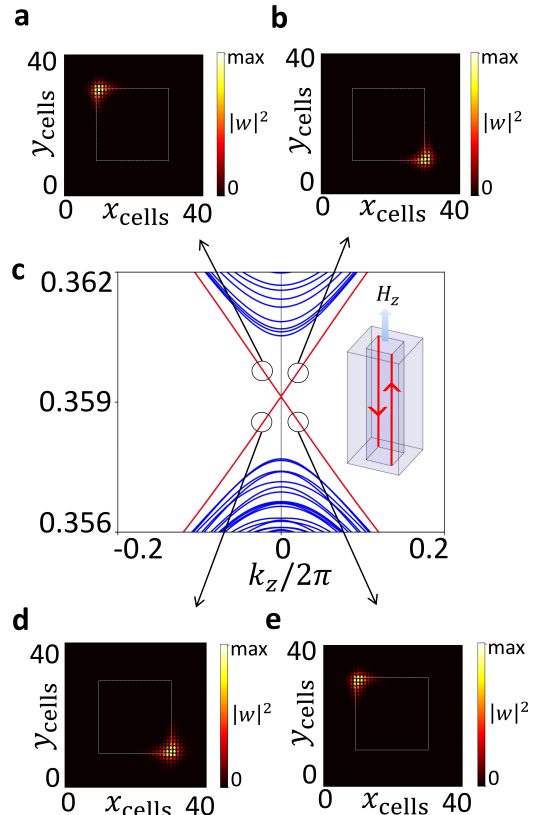


FIG. 5. Gapless AXI hinge states evaluated a z -wire configuration, with $2N_x \times 2N_y = 40 \times 40$ cells. The crystal structure is fully connected but presents an axion phase discontinuity of $\delta\theta \equiv \delta\phi = \pi$. Projected surface bands in blue, hinge bands in red, in panel (c). The chiral modes are localized on \mathcal{I} -related hinges: a xy -cross section of the z -wire geometry is shown in panels (a,b,d,e). The flipping of the external H_z field results in an overall exchange of the group velocity signs. These HOTI states are consistent with the existence of a single unidirectional mode wrapping around a central phase-obstructed core.

As shown in Fig. 5(c), chiral gapless modes emerge as in-gap states in the projected domain-wall bands, consistent with the bulk-hinge correspondence of the photonic r AXI. These HOTI states are consistent with the existence of a single unidirectional mode wrapping around a central phase-obstructed core. Moreover, their group velocity can be easily switched by flipping of the external magnetic bias H_z . Displayed for a cross-section of the connected structure in Fig. 5(a-e), the 1D channels

localize on \mathcal{I} -related hinges parallel to the z direction.

It is noteworthy that not all of the four \mathcal{I} -related hinges support chiral modes at once. Instead, the localization on either a pair of \mathcal{I} -related hinges or the other can be chosen by rotation of the small $h_{x,y}$ bias in the xy plane, leading to 4 possible realizations of the hinges, α, β (with occupancy of the hinges passing through the corners on the 110 diagonal) and γ, δ (with occupancy of the hinges passing through the corners on the $\bar{1}\bar{1}0$ diagonal), as shown in Fig. 6(b-e). These different hinge-state configurations are plotted in Fig. 6 at the Γ point for the upwards-moving state. As shown in the Supplementary Notes, they can be regarded as distinct boundary-obstructed phases [56, 57], since a surface gap (but not a bulk gap) must close in passing from one configuration to another.

The $\alpha, \beta, \gamma, \delta$ gyrotropic-bias-field induced transitions offer a promising and physically accessible way to manipulate the photonic 1D modes, via rotation of the PhC gyrotropic axis through magnetic control by external field. Therefore, the present platform can provide an effective photonic topological switch between different 1D photonic fiber configurations.

Remarkably, the observed hinge modes are embedded within a fully connected 3D dielectric structure, making them highly suitable for guided-light communication applications, as they are protected from radiation through the electromagnetic continuum [38].

By proposing the first tunable HOTI chiral hinge states in PhCs [39], we provide a PhC realization and a distinct manifestation of the axionic hinge states predicted in supercell-modulated Weyl semimetals [24–26, 35, 55].

More specifically, the hinge modes of Fig. 5(b-e) are consistent with the presence of a single, unidirectional axionic mode wrapping around a central phase-obstructed core [58].

CONCLUSIONS

In conclusion, we proposed a novel design strategy to induce axionic band topology in a gyrotropic PhC and demonstrated the potential use for magnetically-tunable photonic switch devices. This approach provides a realistic and physically accessible platform for generating and manipulating the higher order topology of the AXI PhC, enabling effective topological switching between different axionic hinge of light configurations. In addition to its fundamental theoretical significance, related to the possibility of coupling between photonic axionic excitations and dark-matter axions, the realization of AXI PhC has the potential to open up the field of axion-based topology, enabling more efficient and versatile control of light propagation in photonic crystals, and thus advancing the state-of-the-art in photonic communication and optical technologies.

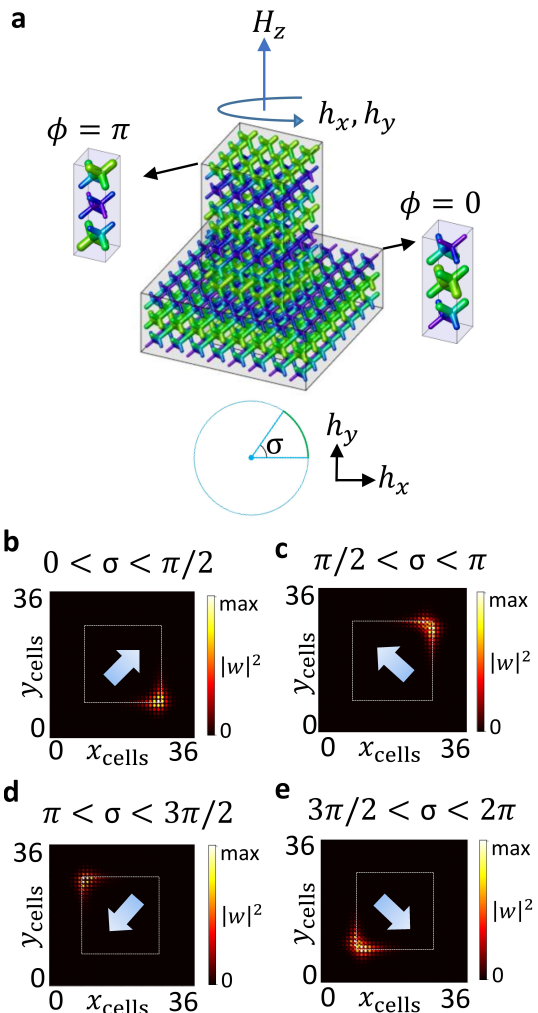


FIG. 6. Tunable AXI hinge states at Γ , for different magnetic bias configurations, computed via the TETB. Panel (a) displays the corresponding PhC dielectric structure. For visual purposes, the central $\phi = 0$ core is extruded vertically with respect to the phase-obstructed embedding with $\phi = \pi$. Panels (b-e) correspond to $\alpha, \gamma, \beta, \delta$ configurations. A single eigenvector is plotted here, upwards moving. The activation of the 90° -rotated hinges is made possible via a $h_{x,y}$ in-plane small bias component.

METHODS

Transversality-Enforced Tight-Binding model for a supercell-modulated PhC. To efficiently simulate the electromagnetic response of the photonic r AXI, we develop a transversality-enforced tight-binding model (TETB) [42], capable of capturing and regularizing the Γ -point electromagnetic obstruction that arises due to the transversality constraint of the Maxwell equations [42, 43]. The model allows the demonstration of HOTI bulk-hinge correspondence of the r AXI through cost-effective calculations of large-scale slab- and rod-geometries. The underlying PhCs that constitute the

starting point of our *r*AXI design are the gyrotropic Weyl semimetals shown of Fig. 1(a). Before the introduction of the *z*-directed external magnetic field and SM, the crystal structure belongs to space group (SG) #224 (*Pn3m*) [33, 34, 42].

The symmetry content of the photonic bands can be deduced by analyzing the Bloch electric modes (\mathbf{E}), obtained in MPB via numerical solution of the Maxwell equations. The \mathbf{E} field transforms as a vector:

$$g\mathbf{E}(\mathbf{r}) = (R\mathbf{E})(R^{-1}(\mathbf{r} - \mathbf{t})), \quad (\text{M.0})$$

for each space group operation $g = \{R|\mathbf{t}\}$, where R is a point group element and \mathbf{t} a translation.

For each n band with $\omega \neq 0$ and every high-symmetry point \mathbf{k}_h , we compute the $x_{n,\mathbf{k}_h}(g)$ diagonal elements of the representation matrix corresponding to g in the little group of \mathbf{k}_h , from the overlap integrals:

$$x_{n,\mathbf{k}}(g) = \langle \mathbf{E}_{n,\mathbf{k}_h} | g\mathbf{D}_{n,\mathbf{k}_h} \rangle \quad (\text{M.1})$$

where $\mathbf{D} = \varepsilon\mathbf{E}$ is the displacement field and ε the dielectric constant. From the Schur's Orthogonality Relations [59], we are able to extract the symmetry vector \mathbf{v}^T that gives the multiplicity irreducible representation (irrep) in the little group of each high symmetry point. We label the irrep accordingly to the notation of Bilbao Crystallographic Server (BCS) [60]

This analysis returns, for the six lowest-electromagnetic modes:

$$\mathbf{v}^T = [(\blacksquare)^{2T} + \Gamma_2^- + \Gamma_4^-, R_4^- + R_5^+, M_1 + 2M_4, X_1 + X_3 + X_4] \quad (\text{M.2})$$

where $(\blacksquare)^{2T}$ indicates the irregular symmetry content at Γ and $\omega = 0$ arising from transversality of the electromagnetic waves [42, 43], with $()^T$ labeling the transverse bands.

A symmetry-constrained, tight-binding Hamiltonian $H(\mathbf{k})$ can be constructed for these transverse photonic bands, via the TETB methods proposed by Ref. [42]. This approach proceeds with the introduction of auxiliary longitudinal modes \mathbf{v}^L , able to regularize the Γ -point obstruction, in order for $\mathbf{v}^{T+L} = \mathbf{v}^T + \mathbf{v}^L$ to be regular. By exploiting a formal mapping between the Schrödinger and electromagnetic wave equations, which relates energies and frequencies quadratically ($\lambda \sim \omega^2$, see [61]), a TETB model is developed enforcing the lowest set of longitudinal bands at $\omega^2 \leq 0$, resulting in the $\mathbf{v}^T = \mathbf{v}^{T+L} - \mathbf{v}^L$ transverse vector capturing all the symmetry, topology and energetic features of the active bands in the PhC. For the specific \mathbf{v}^T of Eq. M2, this can be achieved via

$$\mathbf{v}^{T+L} = A_{2u}@4b + A_{2u}@4c. \quad (\text{M.3})$$

with $\mathbf{v}^L = A_1@2a$, where the decomposition is done in terms of elementary band representations (EBRs), which

constitute the trivial atomic limits induced by a localized orbital at a specific Wyckoff position, as in the notation of BCS. This results in a 8-band model, from A_{2u} photonic pseudo-orbitals at Wyckoff position $4b$ and $4c$. Gyrotropy can be as well modeled via non-minimal coupling to an external magnetic field \mathbf{H} :

$$H(\mathbf{k}, \mathbf{H}) = H(\mathbf{k}) + f(\mathbf{k}, \mathbf{H}), \quad (\text{M.4})$$

where the function $f(\mathbf{k}, \mathbf{H})$ should respect the symmetries of the crystal, \mathbf{H} transforming as a pseudovector. Non-minimal coupling is adopted, due to the uncharged nature of photons, which prevents the use of Peierls substitution. The $\mathbf{H} = (0, 0, H_z)$ field is tuned in order for a Weyl dipole to form along the k_z line, with a separation of $|\mathbf{Q}| = |\mathbf{q}_+ - \mathbf{q}_-| = 2\pi/N$ and $N \in \mathbb{N}$ and $N \geq 2$, as shown in Fig. 1(a).

Starting from the $H(\mathbf{k}, \mathbf{H})$ magnetic Hamiltonian, we consider an additional perturbation aiming to capture the effect of a SM of the dielectric elements. The perturbation is introduced as a *z*-periodic on-site potential of Wyckoff positions $4b$ and $4c$:

$$H_\Delta(\mathbf{r}, \mathbf{H}) = H(\mathbf{r}, \mathbf{H}) + \sum_i V_i \cos\left(\frac{2\pi z_i}{N|a|} + \phi\right) c_i^\dagger(\mathbf{r})c_i(\mathbf{r}), \quad (5)$$

where $H(\mathbf{r}, \mathbf{H})$ is the real-space TETB Hamiltonian for the magnetic system before modulation, $|a|$ is the lattice parameter of the crystal before SM, and V_i and ϕ parameterize the amplitude and the phase of the modulation, respectively. Note that the sum in Eq. (5) runs over all the basis pseudo-orbitals used in the TETB model, i.e., the pseudo-orbitals placed at WPs $4c$ and $4b$. Since this positions are related by symmetry, the amplitude of the modulation in the positions inside a WP should be equal. We will call them V_{4c} and V_{4b} , respectively.

However, since maximal Wyckoff position $4b$ and $4c$ cannot be adiabatically deformed into each other without breaking the symmetry of the model, we have the additional freedom of choosing the relative sign of their modulation amplitude, V_{4b} and V_{4c} . Justified by the fact that Wyckoff positions $4c$ fall inside the dielectric elements, while Wyckoff positions $4b$ are in the air region, we decide to adopt the convention where the on-site potentials on $4b$ and $4c$ are opposite in sign, i.e. $V_{4c} = -V_{4b} > 0$, consistent with regions of higher and lower electromagnetic energy concentration. As shown in Fig. 1(c), the effect of the SM is correctly captured by the transverse modes of the TETB after the introduction of the on-site potential, which results in the opening of a $C_z = 1$ gap.

TETB symmetry vectors, double-band inversion and symmetry-constrained Γ -content As we will demonstrate now, the supercell-modulated pseudo-orbitals of the TETB induce all the irreps of the supercell-modulated PhC band-structure, representing an exact representation for the $\tilde{\mathbf{v}}_\phi^T$ electromagnetic modes

below the gap, $\tilde{\mathbf{v}}$ standing for the symmetry vector after modulation. Note that we express the symmetry vector in the notation of MSG #2.4 ($P\bar{1}$), which is the symmetry of the crystal after the introduction of the H_z magnetic bias, the \mathcal{I} -symmetric SM and the off-axis $h_{x,y}$ perturbation. For the geometry-modulated PhCs, we find:

$$\begin{aligned} \tilde{\mathbf{v}}_{\phi=0}^T &= [(\blacksquare)^{2T} + 2\Gamma_1^+ + 2\Gamma_1^-, 2R_1^+ + 4R_1^-, \\ &3T_1^+ + 3T_1^-, 3U_1^+ + 3U_1^-, 2V_1^+ + 4V_1^-, \\ &3X_1^+ + 3X_1^-, 3Y_1^+ + 3Y_1^-, 3Z_1^+ + 3Z_1^-] \end{aligned} \quad (\text{M.6})$$

and

$$\begin{aligned} \tilde{\mathbf{v}}_{\phi=\pi}^T &= [(\blacksquare)^{2T} + 2\Gamma_1^+ + 2\Gamma_1^-, 2R_1^+ + 4R_1^-, \\ &3T_1^+ + 3T_1^-, 3U_1^+ + 3U_1^-, 4V_1^+ + 2V_1^-, \\ &3X_1^+ + 3X_1^-, 3Y_1^+ + 3Y_1^-, 3Z_1^+ + 3Z_1^-] \end{aligned} \quad (\text{M.7})$$

On the other side, for the onsite-modulated TETB, we obtain:

$$\begin{aligned} \tilde{\mathbf{v}}_{\phi=0}^{T+L} &= [4\Gamma_1^+ + 8\Gamma_1^-, 5R_1^+ + 7R_1^-, \\ &6T_1^+ + 6T_1^-, 6U_1^+ + 6U_1^-, 5V_1^+ + 7V_1^-, \\ &6X_1^+ + 6X_1^-, 6Y_1^+ + 6Y_1^-, 6Z_1^+ + 6Z_1^-] \end{aligned} \quad (\text{M.8})$$

and

$$\begin{aligned} \tilde{\mathbf{v}}_{\phi=\pi}^{T+L} &= [4\Gamma_1^+ + 8\Gamma_1^-, 5R_1^+ + 7R_1^-, \\ &6T_1^+ + 6T_1^-, 6U_1^+ + 6U_1^-, 7V_1^+ + 5V_1^-, \\ &6X_1^+ + 6X_1^-, 6Y_1^+ + 6Y_1^-, 6Z_1^+ + 6Z_1^-] \end{aligned} \quad (\text{M.9})$$

The TETB therefore correctly models the double band inversion occurring at the $V = (\pi, \pi, 0)$ point, between the system with $\phi = 0$ and $\phi = \pi$.

After having identified the irregular irrep content at Γ , as $(\blacksquare)^{2T} = -\Gamma_1^+ + 3\Gamma_1^-$, consistent with symmetry-constrained decomposition for point group $\bar{1}$ as in Refs. [42, 43], we can split the TETB as follows: $\tilde{\mathbf{v}}_{\phi}^{T+L} = \tilde{\mathbf{v}}_{\phi}^T + \tilde{\mathbf{v}}_{\phi}^L$, where:

$$\begin{aligned} \tilde{\mathbf{v}}_{\phi=0,\pi}^L &= [3\Gamma_1^+ + 3\Gamma_1^-, 3R_1^+ + 3R_1^-, \\ &3T_1^+ + 3T_1^-, 3U_1^+ + 3U_1^-, 3V_1^+ + 3V_1^-, \\ &3X_1^+ + 3X_1^-, 3Y_1^+ + 3Y_1^-, 3Z_1^+ + 3Z_1^-] \end{aligned} \quad (\text{M.10})$$

represents the longitudinal auxiliary modes with $\omega^2 < 0$, and has the same expression for both $\phi = 0, \pi$. This shows that the symmetry vector of the TETB represents a precise representation of the electromagnetic modes below the gap of the r AXI. Specifically, the TETB symmetry vector with an onsite supercell-modulation can be decomposed as a longitudinal component $\tilde{\mathbf{v}}_{\phi}^L$ which has same expression for both $\phi = 0, \pi$ phases and a transverse part $\tilde{\mathbf{v}}_{\phi}^T$, which coincides with symmetry vector of the transverse modes of the PhC. As we will verify in

the next section, $\tilde{\mathbf{v}}_{\phi}^L$ has trivial SI, so that the SI of the TETB model and of the MPB solutions coincide.

Magnetic symmetry-indicators for the \mathcal{I} -invariant photonic r AXI. In order to assess the role of \mathcal{I} -symmetry in the quantization of an *relative* axion chemistry (TQC) for non-fermionic systems [42, 43, 54, 62–64] and analyze the symmetry indicators of the modulated PhCs, as the SM angle ϕ is varied. In particular, we consider the structures with $\phi = 0$ and $\phi = \pi$, in presence of both H_z and a small in-plane $h_{x,y}$ which reduce the symmetry to MSG 2.4 (in the BNS notation of Refs. [65, 66]), and we evaluate the $\{\bar{z}_{2,x}, \bar{z}_{2,y}, \bar{z}_{2,z} | \bar{z}_4\}$ magnetic SI [18, 48–51].

For the effective photonic TETB, which is regular and does not present any obstruction at Γ , the calculation of the SI follows directly from the well-known closed-formula expression that relates the \mathcal{I} -eigenvalues to the $\{\bar{z}_{2,x}, \bar{z}_{2,y}, \bar{z}_{2,z} | \bar{z}_4\}$ magnetic SI [18, 48–51], i.e.:

$$\bar{z}_{2,i} = \frac{1}{2} \sum_{\substack{\mathbf{k}_h \in \{IIMS\} \\ \mathbf{k}_h \cdot \mathbf{R}_i = \pi}} (n_h^+ - n_h^-) \pmod{2} \quad (\text{M.11})$$

$$\bar{z}_4 = \frac{1}{2} \sum_{\mathbf{k}_h \in \{IIMS\}} (n_h^+ - n_h^-) \pmod{4} \quad (\text{M.12})$$

where n_h^+ (n_h^-) are the multiplicities of the positive (negative) parity eigenvalues at the high-symmetry point \mathbf{k}_h , and \mathbf{R}_i are the primitive lattice vectors. This returns, depending on the phase ϕ :

$$\nu_{\phi=0}^{T+L} = \{0, 0, 1|0\} \quad (\text{M.13})$$

and

$$\nu_{\phi=\pi}^{T+L} = \{0, 0, 1|2\}. \quad (\text{M.14})$$

To obtain the corresponding ν_{ϕ}^T transverse SI for the electromagnetic modes, we can exploit the linearity of the SI with respect to the symmetry vector [43, 67], i.e.:

$$\nu_i^T = \nu_i^{L+T} - \nu_i^L. \quad (\text{M.15})$$

Since the SI of the longitudinal modes of Eq. M10 are trivial, it follows that the SI of the TETB and the MPB calculations coincide, $\nu_i^T = \nu_i^{L+T}$. This confirms that the $\phi = 0$ and the $\phi = \pi$ systems are obstructed with respect to each other, with a $\delta\bar{z}_4 = 2$ discontinuity of the *even* \bar{z}_4 signaling *relative* axion topology.

Acknowledgements

A.G.E., A.M.P and C.D. acknowledges support from the Spanish Ministerio de Ciencia e Innovación (PID2019-109905GA-C2) and by the Gipuzkoa Provincial Council within the QUAN-000021-01 project.

M.G.D., R.I., A.M.P. and M.G.V. acknowledge the Spanish Ministerio de Ciencia e Innovacion (grant PID2019-109905GB-C21). A.G.E. and M.G.V. acknowledge funding from the IKUR Strategy under the collaboration agreement between Ikerbasque Foundation and DIPC on behalf of the Department of Education of the Basque Government, Programa de ayudas de apoyo a los agentes de la Red Vasca de Ciencia, Tecnología e Innovación acreditados en la categoría de Centros de Investigación Básica y de Excelencia (Programa BERC) from the Departamento de Universidades e Investigación del Gobierno Vasco and Centros Severo Ochoa AEI/CEX2018-000867-S from the Spanish Ministerio de Ciencia e Innovación. M.G.V. thanks support to the Deutsche Forschungsgemeinschaft (DFG, German Research Foundation) GA 3314/1-1 – FOR 5249 (QUAST) and partial support from European Research Council (ERC) grant agreement no. 101020833. The work of JLM has been supported in part by the Basque Government Grant No. IT1628-22 and the PID2021-123703NB-C21 grant funded by MCIN/AEI/10.13039/501100011033/ and by ERDF; “A way of making Europe”. The work of B.B. and Y. H. is supported by the Air Force Office of Scientific Research under award number FA9550-21-1-0131. Y. H. received additional support from the US Office of Naval Research (ONR) Multidisciplinary University Research Initiative (MURI) grant N00014-20-1-2325 on Robust Photonic Materials with High-Order Topological Protection. C.D. acknowledges financial support from the MICIU through the FPI PhD Fellowship CEX2018-000867-S-19-1. M.G.D. acknowledges financial support from Government of the Basque Country through the pre-doctoral fellowship PRE_2022_2.0044.

* chiara.devescovi@dipc.org

† aitzolgarcia@dipc.org

‡ maia.vergniorj@cphys.mpg.de

- [1] Frank Wilczek. Two applications of axion electrodynamics. *Physical review letters*, 58(18):1799, 1987.
- [2] Liang Fu, Charles L Kane, and Eugene J Mele. Topological insulators in three dimensions. *Physical review letters*, 98(10):106803, 2007.
- [3] Taylor L Hughes, Emil Prodan, and B Andrei Bernevig. Inversion-symmetric topological insulators. *Physical Review B*, 83(24):245132, 2011.
- [4] Ari M Turner, Yi Zhang, Roger SK Mong, and Ashvin Vishwanath. Quantized response and topology of magnetic insulators with inversion symmetry. *Physical Review B*, 85(16):165120, 2012.
- [5] Chen Fang, Matthew J Gilbert, and B Andrei Bernevig. Bulk topological invariants in noninteracting point group symmetric insulators. *Physical Review B*, 86(11):115112, 2012.
- [6] Benjamin J Wieder and B Andrei Bernevig. The axion insulator as a pump of fragile topology. *arXiv preprint arXiv:1810.02373*, 2018.
- [7] Xiao-Liang Qi, Rundong Li, Jiadong Zang, and Shou-Cheng Zhang. Inducing a magnetic monopole with topological surface states. *science*, 323(5918):1184–1187, 2009.
- [8] Akihiko Sekine and Kentaro Nomura. Axion electrodynamics in topological materials. *Journal of Applied Physics*, 129(14):141101, 2021.
- [9] Liang Wu, M Salehi, N Koirala, J Moon, S Oh, and NP Armitage. Quantized faraday and kerr rotation and axion electrodynamics of a 3d topological insulator. *Science*, 354(6316):1124–1127, 2016.
- [10] Nicodemos Varnava and David Vanderbilt. Surfaces of axion insulators. *Physical Review B*, 98(24):245117, 2018.
- [11] Rafael González-Hernández, Carlos Pinilla, and Bernardo Uribe. Axion insulators protected by c_2t symmetry, their k -theory invariants, and material realizations. *Physical Review B*, 106(19):195144, 2022.
- [12] Fan Zhang, Charles L Kane, and Eugene J Mele. Surface state magnetization and chiral edge states on topological insulators. *Physical Review Letters*, 110(4):046404, 2013.
- [13] Changming Yue, Yuanfeng Xu, Zhida Song, Yuan-Ming Lu, Hongming Weng, Chen Fang, and Xi Dai. Symmetry enforced chiral hinge states and surface quantum anomalous hall effect in magnetic axion insulator. *arXiv preprint arXiv:1807.01414*, 2018.
- [14] Eslam Khalaf. Higher-order topological insulators and superconductors protected by inversion symmetry. *Physical Review B*, 97(20):205136, 2018.
- [15] Yuanfeng Xu, Zhida Song, Zhijun Wang, Hongming Weng, and Xi Dai. Higher-order topology of the axion insulator $e_{\text{uin}} 2$ as 2 . *Physical review letters*, 122(25):256402, 2019.
- [16] Thomas Olsen, Tomáš Rauch, David Vanderbilt, and Ivo Souza. Gapless hinge states from adiabatic pumping of axion coupling. *Physical Review B*, 102(3):035166, 2020.
- [17] Yutaro Tanaka, Ryo Takahashi, Tiantian Zhang, and Shuichi Murakami. Theory of inversion- z_4 protected topological chiral hinge states and its applications to layered antiferromagnets. *Physical Review Research*, 2(4):043274, 2020.
- [18] Ryo Takahashi, Yutaro Tanaka, and Shuichi Murakami. Bulk-edge and bulk-hinge correspondence in inversion-symmetric insulators. *Physical Review Research*, 2(1):013300, 2020.
- [19] Ming Gong, Haiwen Liu, Hua Jiang, Chui-Zhen Chen, and XC Xie. Half-quantized helical hinge currents in axion insulators. *arXiv preprint arXiv:2203.12982*, 2022.
- [20] Frank Schindler, Zhijun Wang, Maia G Vergniory, Ashley M Cook, Anil Murani, Shamashis Sengupta, Alik Yu Kasumov, Richard Deblock, Sangjun Jeon, Ilya Drozdov, et al. Higher-order topology in bismuth. *Nature physics*, 14(9):918–924, 2018.
- [21] Frank Schindler, Ashley M Cook, Maia G Vergniory, Zhijun Wang, Stuart SP Parkin, B Andrei Bernevig, and Titus Neupert. Higher-order topological insulators. *Science advances*, 4(6):eaat0346, 2018.
- [22] Nicodemos Varnava, Ivo Souza, and David Vanderbilt. Axion coupling in the hybrid wannier representation. *Physical Review B*, 101(15):155130, 2020.
- [23] Dan Sehayek, Manisha Thakurathi, and AA Burkov. Charge density waves in weyl semimetals. *Physical Review B*, 102(11):115159, 2020.
- [24] Yizhi You, Gil Young Cho, and Taylor L Hughes. Re-

- sponse properties of axion insulators and weyl semimetals driven by screw dislocations and dynamical axion strings. *Physical Review B*, 94(8):085102, 2016.
- [25] Johannes Gooth, Barry Bradlyn, Shashank Honnali, Clemens Schindler, Nitesh Kumar, Jonathan Noky, Yangpeng Qi, Chandra Shekhar, Yan Sun, Zhijun Wang, et al. Axionic charge-density wave in the weyl semimetal (tase4) 2i. *Nature*, 575(7782):315–319, 2019.
- [26] Zhong Wang and Shou-Cheng Zhang. Chiral anomaly, charge density waves, and axion strings from weyl semimetals. *Physical Review B*, 87(16):161107, 2013.
- [27] So Chigusa, Takeo Moroi, and Kazunori Nakayama. Axion/hidden-photon dark matter conversion into condensed matter axion. *Journal of High Energy Physics*, 2021(8):1–33, 2021.
- [28] David JE Marsh, Kin Chung Fong, Erik W Lentz, Libor Šmejkal, and Mazhar N Ali. Proposal to detect dark matter using axionic topological antiferromagnets. *Physical Review Letters*, 123(12):121601, 2019.
- [29] Rundong Li, Jing Wang, Xiao-Liang Qi, and Shou-Cheng Zhang. Dynamical axion field in topological magnetic insulators. *Nature Physics*, 6(4):284–288, 2010.
- [30] Alexander J Millar, Georg G Raffelt, Javier Redondo, and Frank D Steffen. Dielectric haloscopes to search for axion dark matter: theoretical foundations. *Journal of Cosmology and Astroparticle Physics*, 2017(01):061, 2017.
- [31] Matthew Lawson, Alexander J Millar, Matteo Pancaldi, Edoardo Vitagliano, and Frank Wilczek. Tunable axion plasma haloscopes. *Physical review letters*, 123(14):141802, 2019.
- [32] Naoto Yokoi and Eiji Saitoh. Stimulated emission of dark matter axion from condensed matter excitations. *Journal of High Energy Physics*, 2018(1):1–21, 2018.
- [33] Chiara Devescovi, Mikel García-Díez, Iñigo Robredo, María Blanco de Paz, Jon Lasa-Alonso, Barry Bradlyn, Juan L Mañes, Maia G Vergniory, and Aitzol García-Etxarri. Cubic 3d chern photonic insulators with orientable large chern vectors. *Nature communications*, 12(1):1–12, 2021.
- [34] Chiara Devescovi, Mikel Garcia-Diez, Barry Bradlyn, Juan Luis Mañes, Maia G Vergniory, and Aitzol Garcia-Etxarri. Vectorial bulk-boundary correspondence for 3d photonic chern insulators. *arXiv preprint arXiv:2206.04147*, 2022.
- [35] Benjamin J Wieder, Kuan-Sen Lin, and Barry Bradlyn. Axionic band topology in inversion-symmetric weyl-charge-density waves. *Physical Review Research*, 2(4):042010, 2020.
- [36] Wujun Shi, Benjamin J Wieder, Holger L Meyerheim, Yan Sun, Yang Zhang, Yiwei Li, Lei Shen, Yanpeng Qi, Lexian Yang, Jagannath Jena, et al. A charge-density-wave topological semimetal. *Nature Physics*, 17(3):381–387, 2021.
- [37] Hidetoshi Fukuyama and Patrick A Lee. Dynamics of the charge-density wave. i. impurity pinning in a single chain. *Physical Review B*, 17(2):535, 1978.
- [38] John D Joannopoulos, Steven G Johnson, Joshua N Winn, and Robert D Meade. *Molding the flow of light*. Princeton. Univ. Press. Princeton, NJ [ua], 2008.
- [39] Minkyung Kim, Zubin Jacob, and Junsuk Rho. Recent advances in 2d, 3d and higher-order topological photonics. *Light: Science & Applications*, 9(1):130, 2020.
- [40] Gui-Geng Liu, Zhen Gao, Qiang Wang, Xiang Xi, Yuan-Hang Hu, Maoren Wang, Chengqi Liu, Xiao Lin, Longjiang Deng, Shengyuan A Yang, et al. Topological chern vectors in three-dimensional photonic crystals. *Nature*, 609(7929):925–930, 2022.
- [41] Xiang Xi, Bei Yan, Linyun Yang, Yan Meng, Zhen-Xiao Zhu, Jing-Ming Chen, Ziyao Wang, Peiheng Zhou, Perry Ping Shum, Yihao Yang, et al. Topological antichiral surface states in a magnetic weyl photonic crystal. *Nature Communications*, 14(1):1991, 2023.
- [42] Antonio Morales Perez, Chiara Devescovi, Yoonseok Hwang, Mikel Garcia Diez, Barry Bradlyn, Juan Luis Manes, Maia Garcia Vergniory, and Aitzol Garcia Etxarri. Transversality-enforced tight-binding model for 3d photonic crystals aided by topological quantum chemistry. *arXiv:2305.18257*.
- [43] Thomas Christensen, Hoi Chun Po, John D Joannopoulos, and Marin Soljačić. Location and topology of the fundamental gap in photonic crystals. *Physical Review X*, 12(2):021066, 2022.
- [44] Zhaoju Yang, Meng Xiao, Fei Gao, Ling Lu, Yidong Chong, and Baile Zhang. Weyl points in a magnetic tetrahedral photonic crystal. *Optics express*, 25(14):15772–15777, 2017.
- [45] FDM Haldane and S Raghu. Possible realization of directional optical waveguides in photonic crystals with broken time-reversal symmetry. *Physical review letters*, 100(1):013904, 2008.
- [46] Srinivas Raghu and Frederick Duncan Michael Haldane. Analogs of quantum-hall-effect edge states in photonic crystals. *Physical Review A*, 78(3):033834, 2008.
- [47] Steven G Johnson and John D Joannopoulos. Block-iterative frequency-domain methods for maxwell’s equations in a planewave basis. *Optics express*, 8(3):173–190, 2001.
- [48] Haruki Watanabe, Hoi Chun Po, and Ashvin Vishwanath. Structure and topology of band structures in the 1651 magnetic space groups. *Science advances*, 4(8):eaat8685, 2018.
- [49] Heejae Kim, Ken Shiozaki, and Shuichi Murakami. Glide-symmetric magnetic topological crystalline insulators with inversion symmetry. *Physical Review B*, 100(16):165202, 2019.
- [50] Yuanfeng Xu, Luis Elcoro, Zhi-Da Song, Benjamin J Wieder, MG Vergniory, Nicolas Regnault, Yulin Chen, Claudia Felser, and B Andrei Bernevig. High-throughput calculations of magnetic topological materials. *Nature*, 586(7831):702–707, 2020.
- [51] Luis Elcoro, Benjamin J Wieder, Zhida Song, Yuanfeng Xu, Barry Bradlyn, and B Andrei Bernevig. Magnetic topological quantum chemistry. *Nature communications*, 12(1):1–10, 2021.
- [52] Hoi Chun Po. Symmetry indicators of band topology. *Journal of Physics: Condensed Matter*, 32(26):263001, 2020.
- [53] Maria Blanco de Paz, Chiara Devescovi, Geza Giedke, Juan José Saenz, Maia G Vergniory, Barry Bradlyn, Dario Bercioux, and Aitzol García-Etxarri. Tutorial: computing topological invariants in 2d photonic crystals. *Advanced Quantum Technologies*, 3(2):1900117, 2020.
- [54] María Blanco De Paz, Maia G Vergniory, Dario Bercioux, Aitzol García-Etxarri, and Barry Bradlyn. Engineering fragile topology in photonic crystals: Topological quantum chemistry of light. *Physical Review Research*, 1(3):032005, 2019.

- [55] Jeffrey CY Teo and Charles L Kane. Topological defects and gapless modes in insulators and superconductors. *Physical Review B*, 82(11):115120, 2010.
- [56] Eslam Khalaf, Wladimir A Benalcazar, Taylor L Hughes, and Raquel Queiroz. Boundary-obstructed topological phases. *Physical Review Research*, 3(1):013239, 2021.
- [57] Ka Ho Wong, Mark R Hirsbrunner, Jacopo Gliozzi, Arbaz Malik, Barry Bradlyn, Taylor L Hughes, and Dirk K Morr. Higher order topological superconductivity in magnet-superconductor hybrid systems. *arXiv preprint arXiv:2210.15582*, 2022.
- [58] Eslam Khalaf, Hoi Chun Po, Ashvin Vishwanath, and Haruki Watanabe. Symmetry indicators and anomalous surface states of topological crystalline insulators. *Physical Review X*, 8(3):031070, 2018.
- [59] Willard Miller. *Symmetry groups and their applications*. Academic Press, 1973.
- [60] Luis Elcoro, Barry Bradlyn, Zhijun Wang, Maia G Vergniory, Jennifer Cano, Claudia Felser, B Andrei Bernevig, Danel Orobengoa, G Flor, and Mois I Aroyo. Double crystallographic groups and their representations on the Bilbao crystallographic server. *Journal of Applied Crystallography*, 50(5):1457–1477, 2017.
- [61] Giuseppe De Nittis and Max Lein. The schrodinger formalism of electromagnetism and other classical waves—how to make quantum-wave analogies rigorous. *Annals of Physics*, 396:579–617, 2018.
- [62] Juan L Mañes. Fragile phonon topology on the honeycomb lattice with time-reversal symmetry. *Physical Review B*, 102(2):024307, 2020.
- [63] Martín Gutiérrez-Amigo, Maia G Vergniory, Ion Errea, and JL Mañes. Topological phonon analysis of the two-dimensional buckled honeycomb lattice: An application to real materials. *Physical Review B*, 107(14):144307, 2023.
- [64] Yuanfeng Xu, MG Vergniory, Da-Shuai Ma, Juan L Mañes, Zhi-Da Song, B Andrei Bernevig, Nicolas Regnault, and Luis Elcoro. Catalogue of topological phonon materials. *arXiv preprint arXiv:2211.11776*, 2022.
- [65] Christopher Bradley and Arthur Cracknell. *The mathematical theory of symmetry in solids: representation theory for point groups and space groups*. Oxford University Press, 2010.
- [66] NV Belov. Neronova, nn and smirnova t. S., Shubnikov groups. *Sov. Phys./Crystallography*, 2:311–322, 1957.
- [67] Jennifer Cano and Barry Bradlyn. Band representations and topological quantum chemistry. *Annual Review of Condensed Matter Physics*, 12:225–246, 2021.